

Journal of
Applied Remote Sensing

Effect of black carbon on dust property retrievals from satellite observations

Tang-Huang Lin
Ping Yang
Bingqi Yi

Effect of black carbon on dust property retrievals from satellite observations

Tang-Huang Lin,^a Ping Yang,^b and Bingqi Yi^b

^aNational Central University, Center for Space and Remote-sensing Research, Zhongli, Taiwan

^bTexas A&M University, Department of Atmospheric Sciences, College Station, Texas 77843
pyang@tamu.edu

Abstract. The effect of black carbon on the optical properties of polluted mineral dust is studied from a satellite remote-sensing perspective. By including the auxiliary data of surface reflectivity and aerosol mixing weight, the optical properties of mineral dust, or more specifically, the aerosol optical depth (AOD) and single-scattering albedo (SSA), can be retrieved with improved accuracy. Precomputed look-up tables based on the principle of the Deep Blue algorithm are utilized in the retrieval. The mean differences between the retrieved results and the corresponding ground-based measurements are smaller than 1% for both AOD and SSA in the case of pure dust. However, the retrievals can be underestimated by as much as 11.9% for AOD and overestimated by up to 4.1% for SSA in the case of polluted dust with an estimated 10% (in terms of the number-density mixing ratio) of soot aggregates if the black carbon effect on dust aerosols is neglected. © The Authors. Published by SPIE under a Creative Commons Attribution 3.0 Unported License. Distribution or reproduction of this work in whole or in part requires full attribution of the original publication, including its DOI. [DOI: [10.1117/1.JRS.7.073568](https://doi.org/10.1117/1.JRS.7.073568)]

Keywords: black carbon; mineral dust; aerosol optical depth; single-scattering albedo; aerosol mixing weight.

Paper 12341 received Sep. 28, 2012; revised manuscript received Mar. 3, 2013; accepted for publication Mar. 28, 2013; published online May 3, 2013.

1 Introduction

Dust storms are hazardous weather events that frequently occur in Asia and North Africa, particularly during boreal spring and summer. The dust storms lead to the long-range transport of a substantial amount of dust from the desert and semiarid dust sources to the downwind regions.¹⁻⁶ The long-range dust transport can influence the regional and global aerosol loading, radiative energy budget, rainfall pattern, air quality, public health and global climate systems.⁷⁻⁹ Thus, monitoring dust and understanding its effect on atmospheric properties have received a great deal of attention. Due to long-range dust transport, satellite observations are deemed the best approach to delineate the spatial and temporal distributions of airborne dust. Various up-to-date, satellite-based dust storm monitoring techniques have been developed and employed.^{10,11}

Asia and Africa are two major source regions of black carbon, the main component of soot aggregates. These carbon emissions are generally associated with open combustion, such as forest fires, land-clearing by fire, agricultural waste-burning events, and from traditional stoves and kilns. Automobile and industrial emissions also contribute to the emission of black carbon. Airborne dust particles may be coated or attached with carbon from natural and anthropogenic combustion over farmland, forests, and industrial regions. Previous surveys indicate that most Asian dust particles are mixed with soot aggregates,¹²⁻¹⁶ which dramatically alter the physiochemical characteristics of the particles. Thus, there is a pressing need to develop a method to quantitatively assess the black carbon effect on dust optical properties and analyze the radiative properties of polluted dust particles from satellite observations of dust storms.

Numerous studies have been conducted to understand the optical properties of dust particles and soot aggregates,¹⁷⁻²⁸ finding that particle shape is an important physical parameter. As the mineral dust particles are almost exclusively nonspherical,²⁹⁻³¹ the nonsphericity effect has to be taken into account when calculating dust optical properties.³²⁻³⁵ Although dust particle morphologies are complicated, approximating the particles as an ensemble of randomly oriented

spheroids is valid for computing the bulk optical properties for many applications.³⁶ A triaxial ellipsoidal model with one more degree of morphological freedom than the axially rotational spheroid model has also been suggested.³⁷ The results based on an ellipsoidal model with a set of optimal shapes and weights closely agree with laboratory measurements in terms of both the intensity and polarization state of scattered radiation.³⁷ Using the ellipsoidal model and a combination of the Lorenz-Mie theory, T-matrix method, discrete dipole approximation (DDA) and an improved geometric optics method (IGOM), Meng et al.³⁸ developed a database of the single-scattering properties of tri-axial ellipsoidal mineral dust particles for atmospheric radiative transfer simulations and remote-sensing applications. Yi et al.³⁹ utilized the database and showed the importance of the nonsphericity effect of dust-like aerosol on the radiance and flux simulation.

In the study of the optical properties of soot aggregates, Li et al.²⁸ demonstrated that the spherical approximation based on the equivalent volume, equivalent surface area, equivalent ratio of volume to projected area, or radius of gyration, leads to significant errors in the calculation of the optical properties of soot aggregates. To reduce the simulation errors, the fractal aggregates defined by the diffusion-limited cluster-cluster aggregation algorithm (DLCA) are used to derive soot properties. Moreover, the scattering properties of fractal aggregates can be obtained with the Rayleigh-Debye-Gans (RDG) method,⁴⁰ the T-matrix and superposition T-matrix methods,^{41,42} or the generalized multiple Mie (GMM) method.^{43,44}

Dust and soot particles attenuate the incident solar energy through absorption and scattering effects. The key parameters for modeling the extinction efficiency of either mineral dust or airborne soot particles are the complex refractive indices. Although the refractive index values cannot be easily specified after dust and soot mixing, the scattering and absorption properties of aerosols in external or semi-external mixtures have been simulated.^{41,45} The optical properties of a large particle attached with soot clusters can be strongly influenced by the mixing effects. In satellite remote-sensing applications, the single-scattering albedo (SSA) of atmospheric aerosols is important in the forward radiative transfer simulations. This is especially true in retrieving the properties of dust mixed with soot aggregates, because dust aerosols are coarse particles with a strong scattering effect, whereas soot aerosols are fine particles with a strong absorption effect.

This study is intended to understand the effect of soot on the retrieval of the optical properties of polluted dust from moderate resolution imaging spectroradiometer (MODIS) observations based on the principle of the Deep Blue algorithm. The remainder of this paper is organized as follows: Sec. 2 describes the methodology to derive the bulk scattering properties of dust-soot mixture with an external mixture scheme and the radiative transfer model used for the present simulations. The effect of black carbon on the dust properties is discussed in Sec. 3. In Sec. 4 the sensitivity of reflectance at the top of the atmosphere (TOA) to the optical properties of dust-soot mixture is illustrated. The retrievals of the pure and polluted dust AOD and SSA from the MODIS observations are presented and discussed in Sec. 5 and conclusions summarized in Sec. 6.

2 Methodology

2.1 Models for Soot Aggregation and Mineral Dust

The DLCA approximation is employed to define a soot aggregate morphology and to specify the soot particle geometries for the calculation of the single-scattering properties based on the GMM method.^{28,43,44,46} The bulk (ensemble-averaged) optical properties of the particles can be obtained by weighting the probability distribution function (PDF) of the number of monomers per aggregate.

The empirical values of 1.19 and 1.82 for the fractal prefactor and dimension are assumed in the simulation of the soot aggregate geometries.^{24,40} The PDF for the N monomers, $n(N)$, can be expressed as

$$n(N) = \frac{1}{\sqrt{2\pi}N \ln(\sigma_g)} \exp \left\{ - \left[\frac{\ln(N) - \ln(N_g)}{\sqrt{2} \ln(\sigma_g)} \right]^2 \right\}, \quad (1)$$

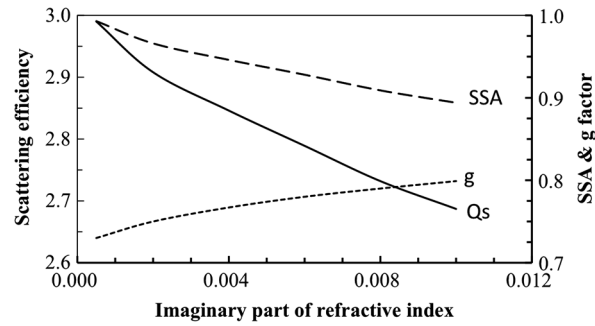


Fig. 1 Simulated scattering efficiency (solid line), SSA (long dashed line), and asymmetry factor (dashed line) of dust at a wavelength of $0.470 \mu\text{m}$.

where N_g is the geometric mean of N , and σ_g is the geometric standard deviation.^{23,47} The values of 200.0 and 2.3 are used for N_g and σ_g ^{28,48} The ensemble-averaged optical properties, for example the phase function and extinction coefficient, can be obtained in the form^{43,44}

$$\bar{P}_{11} = \frac{\int_1^\infty P_{11}(\Theta, N) C^{\text{sca}}(N) n(N) dN}{\int_1^\infty C^{\text{sca}}(N) n(N) dN}, \quad (2)$$

$$\bar{k}^{\text{ext}} = \frac{\int_1^\infty k^{\text{ext}}(N) n(N) dN}{\int_1^\infty n(N) dN}, \quad (3)$$

where \bar{P}_{11} and \bar{k}^{ext} indicate the averaged phase function and the extinction coefficient of an ensemble of aggregates. For an aggregate of N monomers, $P_{11}(\Theta, N)$ and $C^{\text{sca}}(N)$ are the phase function and the scattering cross-section, Θ is the scattering angle, and $k^{\text{ext}}(N)$ is the extinction coefficient in the present study.

The refractive indices of soot aggregates at wavelengths 0.412 , 0.470 and $0.650 \mu\text{m}$ are assumed to be $1.75 + 0.460i$, $1.75 + 0.450i$ and $1.75 + 0.435i$,^{28,41,42,49,50} respectively. The phase functions for individual aggregates, with a set of the monomer numbers (averaged over 100 to 1500 monomers with a 50-monomer increment) at a selected visible wavelength can be computed with the GMM method.

The database software package developed by Meng et al.³⁸ is used for calculating the single-scattering properties of dust-like aerosol particles. Figure 1 shows the variations of mineral dust optical properties with different imaginary parts of the refractive index at $0.470 \mu\text{m}$ when their real part of the refractive index is 1.55. When the imaginary part of the refractive index increases, the scattering efficiency and SSA decrease, while the asymmetry factor increases.

2.2 Mixing Processes

Due to the difficulty in determining the optical properties of internal mixtures, the optical properties of polluted dust particles are derived by an external mixing procedure with each aerosol species represented by its own size distribution and complex refractive index. In this study, the dust refractive indices based on aerosol robotic network (AERONET) retrieval⁵¹⁻⁵³ are used. For external mixing, the extinction coefficient of a combination ($\langle k^{\text{ext}} \rangle$) as a weighted mean of the optical properties of individual components, can be given by Ref. 50,

$$\langle k^{\text{ext}} \rangle = w_d k_d^{\text{ext}} + w_s k_s^{\text{ext}}, \quad (4)$$

where w_d and w_s is the number-density mixing ratio of dust particles and soot aggregates, and $w_d + w_s = 1$; k_d^{ext} and k_s^{ext} are the corresponding extinction coefficients of dust and soot. The asymmetry factor $\langle g \rangle$ and the phase function $\langle P_{11}(\Theta) \rangle$ of the dust-soot mixture can be expressed as

$$\langle g \rangle = \frac{w_d C_d^{\text{sca}} g_d + w_s C_s^{\text{sca}} g_s}{w_d C_d^{\text{sca}} + w_s C_s^{\text{sca}}}, \quad (5)$$

$$\langle P_{11}(\Theta) \rangle = \frac{w_d C_d^{\text{sca}} P_{11_d}(\Theta) + w_s C_s^{\text{sca}} P_{11_s}(\Theta)}{w_d C_d^{\text{sca}} + w_s C_s^{\text{sca}}}, \quad (6)$$

where C_d^{sca} and C_s^{sca} are the scattering cross sections of dust particles and soot aggregates.

To understand the aerosol mixing effect on the single-scattering properties, Liu and Mishchenko⁴¹ simulated the ensemble-averaged photometric characteristics of mixtures formed by soot aggregates and mineral dust. The simulation was conducted at $0.628 \mu\text{m}$ by using the superposition T-matrix method with radii inputs of 0.02 and $1.0 \mu\text{m}$ and refractive indices of $1.75 + 0.435i$ and $1.53 + 0.008i$ for soot monomers and dust particles, respectively. Their simulated ensemble-averaged SSA (0.797 at $0.628 \mu\text{m}$) is close to the present result (0.767 at $0.650 \mu\text{m}$) based on Eqs. (4) to (6), suggesting that the external mixture mechanism used in this study can provide reasonable results. As the irradiance observed at TOA may be varied due to both atmospheric aerosol loading and SSA characteristics, uncertainties in AOD retrievals may be induced if the SSA variation by dust-soot mixing is neglected.

2.3 Simulations of TOA Reflectance

To eliminate the potential errors due to neglecting the radiation polarization state in the simulated spectral radiance/reflectance at the TOA,^{54,55} we employ a polarized radiative transfer code developed by de Haan et al.⁴⁶ employing the adding-doubling principle. In the simulation, the vertical distribution of aerosol loading is divided into seven layers from the surface to the TOA following a Gaussian function with a peak at the height of 3 km above the surface.⁶ Using visible wavelength bands allows the clear-sky atmospheric optical depth ($\tau_{R,\lambda}$) to be calculated as a function of wavelength for the spectral region:⁵⁶

$$\tau_{R,\lambda} = 0.00877\lambda^{-4.05}, \quad (7)$$

where λ is the spectral wavelength in micrometers.

The simulation results of the TOA reflectance ($470 \mu\text{m}$) as a function of the surface reflectance for selected aerosol loadings (AOD = 0.0 and 1.0) and of different SSA values are depicted in Fig. 2(a). Figure 2(b) demonstrates the simulations of the dust-soot mixture with $w_s = 5\%$ soot aggregates. The mineral dust SSA values are reduced by about 1.6% after mixing, and the critical reflectance (vertical dashed lines) changes from 0.155 to 0.135 when the SSA is 0.946 . Here, the critical reflectance is defined as the surface reflectance in the presence of aerosol, but with the TOA reflectance unchanged. It is difficult to infer aerosol property information as the TOA reflectance approaches the critical reflectance, as seen in Fig. 2(c) and 2(d) with surface reflectances of 0.408 and 0.310 , respectively. Both the surface reflectance and the apparent reflectance have the same value as the aerosol loading (AOD) varies between 0.0 and 2.0 . Large errors thus can be incurred in the aerosol property retrievals based on the TOA apparent reflectance at values near the critical reflectance. For instance, the error in the AOD retrieval may be as large as 2.0 under the scenario of Fig. 2(c).

In the satellite observations of the apparent reflectance at the TOA, the atmospheric aerosols generally provide positive radiance contributions over dark surface areas and negative contributions over bright surface areas. The critical reflectance can be used to distinguish dark and bright surfaces. The aerosol contribution is positive when the surface reflectance is less than the critical reflectance (0.408). The relative differences can be noticed in Fig. 2(e). On the contrary, the contributions are negative if the surface reflectance is larger than the critical reflectance value (0.310). When the surface reflectance is larger than the critical reflectance (e.g., 0.4), the differences in the nonaerosol case are negative [Fig. 2(f)]. Therefore, the estimation of the critical reflectance value is crucial for both aerosol retrievals and radiative forcing computations. The

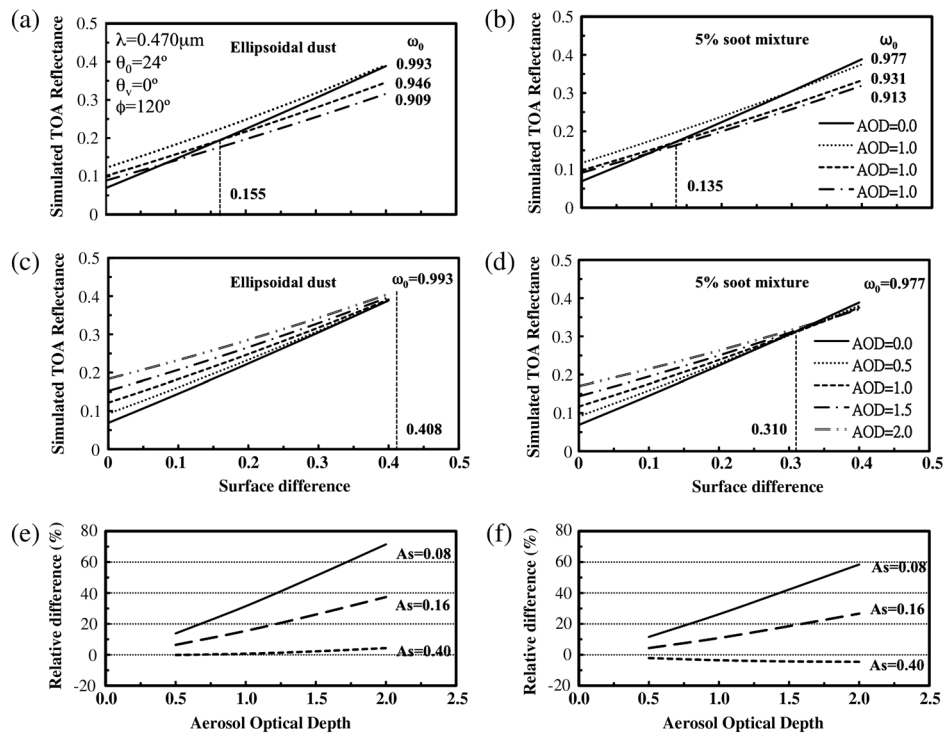


Fig. 2 (a) Simulated TOA reflectance (atmosphere and surface) at $0.470 \mu\text{m}$ and surface reflectance for AOD and SSA (ω_0) based on the triaxial ellipsoidal dust database. The solid line represents the TOA reflectance without aerosol, and the dotted, dashed and long dashed lines are the TOA reflectance under the aerosol loading of AOD = 1.0 with different SSA (ω_0). (b) Same as (a), but mixed with $w_s = 5\%$ soot aggregates. (c) Same as (a), but under the aerosol loading, AOT = 0.0, 0.5, 1.0, 1.5, and 2.0, respectively. (d) Same as (c), but mixed with 5% soot aggregates. (e) The relative difference of TOA reflectance, $[(\text{Refmixture} - \text{Refdust}) / \text{Refdust} \times 100\%]$, from nonaerosol atmosphere in panel (c) when surface reflectance is 0.08 (solid line), 0.16 (long dashed line) and 0.40 (dashed line). (f) Same as (e), but for panel (d).

simulation results indicate the critical reflectance may vary with the atmospheric aerosol SSA, thereby implying the critical reflectance is altered by mixed soot aggregates.

3 Effect of Black Carbon on AOD and SSA Retrievals

The Deep Blue algorithm, originally developed by Hsu et al.^{6,57} for the retrieval of mineral dust optical properties over bright surface areas, is also suitable for analyzing the optical properties of dust-soot mixture. Specifically, a set of look-up tables based on the best match between simulated and observed TOA reflectances at MODIS 0.412-, 0.470-, and 0.650- μm channels are used for retrieving AOD and SSA. Two-channel (0.412 and 0.470 μm) and three-channel (0.412, 0.470, and 0.650 μm) retrieval algorithms are utilized to retrieve dust aerosol properties for low and heavy atmospheric aerosol loading.

The TOA reflectance of mineral dust mixing with different weighted soot aggregates can be simulated by combining aerosol profiles with the aforementioned soot aggregate optical properties, database of mineral dust, and polarized radiative transfer code. With the Deep Blue algorithm, a set of look-up tables of the TOA reflectance (as functions of AOD and SSA) is established for retrieving the optical properties of dust-soot mixtures. In the look-up tables, the TOA reflectance is calculated for a combination of 13 solar zenith angles ($\theta_0 = 0$ deg to 72 deg in 6 deg increments), 14 viewing zenith angles ($\theta_v = 0$ deg to 78 deg in 6 deg increments) and 16 relative azimuthal angles ($\phi = 0$ deg to 180 deg in 12 deg increments). Furthermore, the effective radius and effective variance for mineral dust aerosols are 1.0 μm and 1.0, respectively.

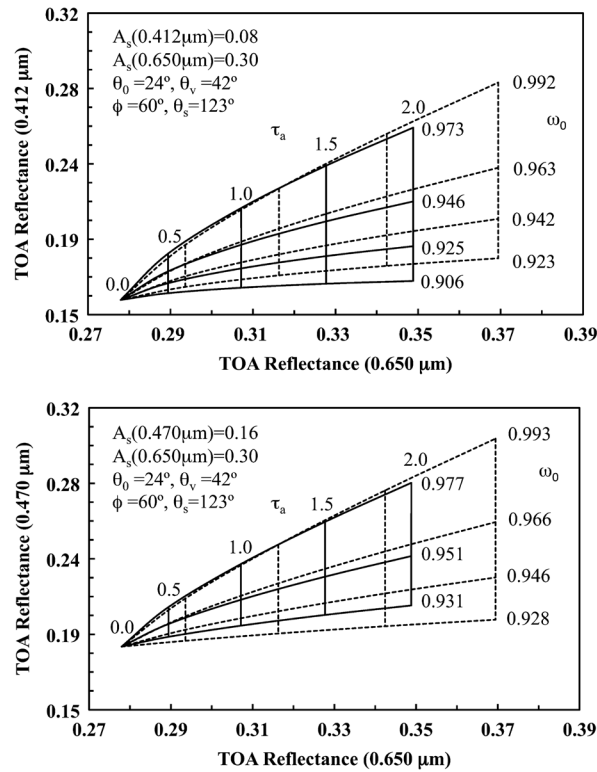


Fig. 3 The simulated TOA reflectance as a function of AOD and SSA for 0.412 versus 0.650 μm (top panel), and 0.470 versus 0.650 μm (lower panel) for mineral dust mixed with (solid line $w_s = 10\%$), and without (dashed line) soot aggregates. The SSA of pure dust and dust-soot mixture aerosols at 0.650 μm are 0.995 and 0.990, respectively.

For the three-channel retrieval technique applied to the simulation scenario with heavy aerosol loading, the look-up tables for the relationships between the simulated TOA apparent reflectances at 0.412 and 0.470 μm, versus those at 0.650 μm as functions of AOD and SSA for pure and polluted dust (dust-soot mixture) aerosols are depicted in Fig. 3. The values of SSA shown in the figures are for the pure dust and dust-soot mixture aerosols at 0.412 (upper panel) and 0.470 μm (lower panel), and the SSA values of pure dust and dust-soot mixture aerosols at 0.650 μm are 0.995 and 0.990, respectively. The look-up tables are constructed based on the relationships between the wavelengths (0.412, 0.470, and 0.650 μm) for simultaneously retrieving the AOD and SSA of aerosols. AOD and SSA retrievals are obviously different between the look-up tables of pure dust (dashed lines) and dust-soot mixture with $w_s = 10\%$ (solid lines), mainly due to the variation in the single-scattering properties. The retrievals of the mixture aerosol properties have the same weakness as in the two-channel model (for the condition of light aerosol loading). The results in Fig. 3 demonstrates that the failure in incorporating the dust aerosols mixing with soot aggregates can lead to substantial errors in retrieving the AOD and SSA of dust-soot mixtures along the pathway of a dust storm through an industrial region. For example, the differences of retrievals between pure dust and polluted dust are 20.0% and 1.15% for AOD and SSA, respectively, when the aerosol loading in AOD is 1.0.

The simulation results show that the major uncertainties in AOD and SSA retrievals for dust aerosols are induced by the variance in the SSA after mixing with soot aggregates. Figure 4 shows the SSA variation with the imaginary part of the refractive index when mineral dust is mixed with $w_s = 5\%$ and $w_s = 10\%$ soot aggregates at 0.412 and 0.470 μm. The simulations indicate the stronger the scattering by the dust particles, the larger the variation in the SSA for the mixture. Specifically, the effect of dust mixing with soot aggregates on SSA values is more significant for large values than for low values. The results (Figs. 3 and 4) show that a 1.5% variation in the SSA value could result in 20% uncertainty in the AOD retrieval by the three-channel retrieval technique.

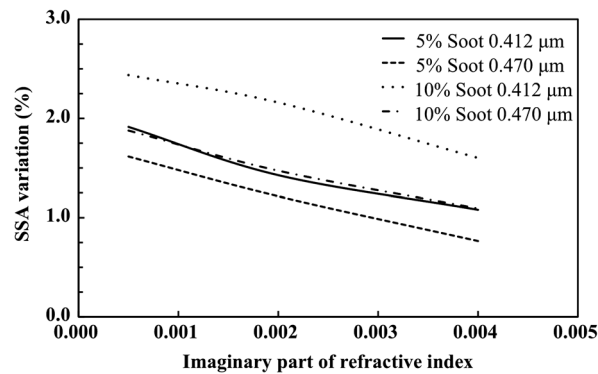


Fig. 4 The variation of SSA versus the imaginary part of refractive index when mineral dust is mixed with $w_s = 5\%$ and $w_s = 10\%$ soot aggregates at $0.412 \mu\text{m}$ and $0.470 \mu\text{m}$.

4 Sensitivity Analysis

4.1 SSA Variance on TOA Reflectance

Figure 5 shows the phase function differences between the pure dust and the dust-soot mixtures with $w_s = 10\%$, which are less than 0.4% . Thus, the change in the TOA reflectance may be mainly due to variations in the SSA.

Figure 6 illustrates the results of the influence of the single-scattering properties on the TOA reflectance at $0.470 \mu\text{m}$ over dark [panels (a), (b), and (c)] and bright surfaces [panels (d), (e), and (f)]. Panels (a) and (d) in Fig. 6 represent the viewing directional TOA reflectance for pure dust, whereas panels (b) and (e) are for the dust-soot mixtures with $w_s = 10\%$. Due to the reduction in the SSA values, the TOA reflectance of the dust-soot mixture is less than that of the pure dust over both dark and bright areas, although the TOA reflectance patterns are quite similar to panels (a), (b), (d), and (e), as shown in Fig. 6. Furthermore, Fig. 6(c) and 6(f) shows the geometric distributions of the relative difference in the apparent reflectivity between the pure dust and dust/soot mixture. By comparing the TOA reflectance difference between the pure dust and the dust-soot mixture, as shown in Fig. 6(a) and 6(b), the geometric distribution of the relative difference can be calculated, which is displayed in Fig. 6(c). The relative difference ranges from 7.2% to 10.6% , and the mean and standard deviations are 9.0% and 2.2% respectively over bright surfaces. Similar results are found over the areas of dark surface.

For most cases, the TOA reflectance and mean relative difference can be determined by the variance in the SSA between the pure dust and the dust-soot mixture (polluted dust), and the standard deviation is attributed to the phase function's difference. More cases are investigated to

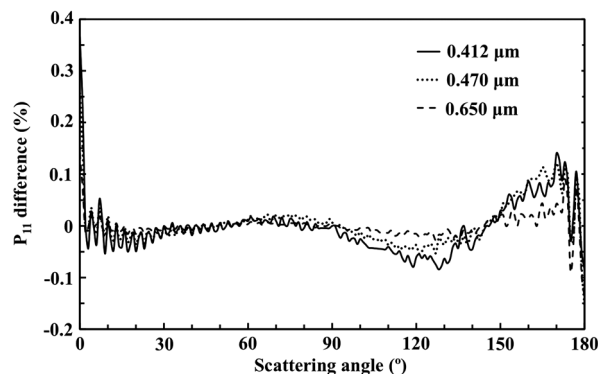


Fig. 5 The phase function differences between dust-soot mixtures (with $w_s = 10\%$ soot aggregates) and pure dust, $[(P_{11\text{dust}} - P_{11\text{mixture}})/P_{11\text{dust}} \times 100\%]$, at $0.412 \mu\text{m}$, $0.470 \mu\text{m}$, and $0.650 \mu\text{m}$.

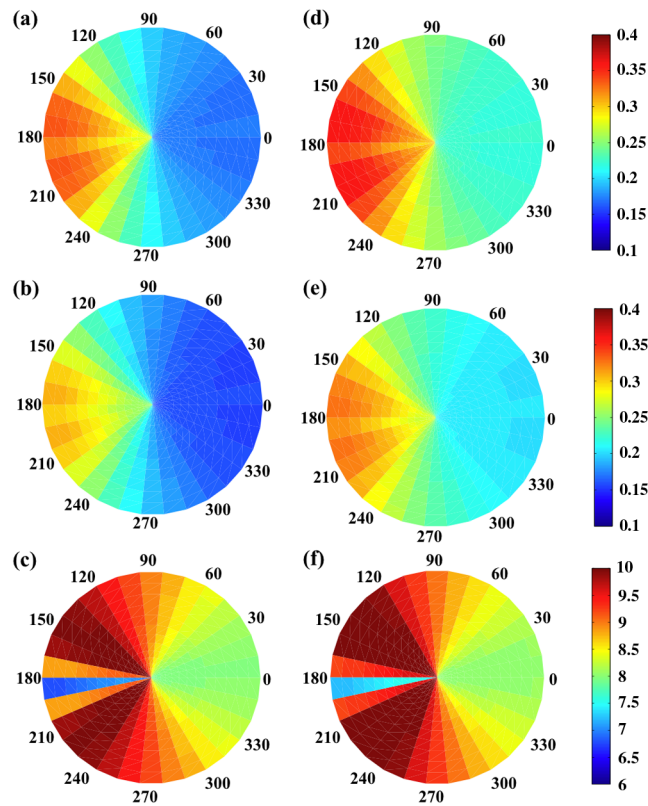


Fig. 6 The azimuthal variations (radius, view zenith angle; angle, relative azimuthal angle) of the apparent reflectance at TOA simulated from the triaxial ellipsoidal dust and soot aggregation models at $0.470 \mu\text{m}$. The solar zenith angle is 24 deg . The AOD and surface reflectance are assumed to be 1.0 and 0.08 [panels (a)–(c)]. Panels (d)–(f) are the results of brighter surface reflectance (0.16). The relative differences in panels (c) and (f) are presented in percentages, $[(\text{Refmixture} - \text{Refdust})/\text{Refdust} \times 100\%]$.

further assess the effect of dust-soot mixtures on the TOA reflectance. SSA and TOA reflectance simulations and the mixing weight of soot aggregates at $0.470 \mu\text{m}$ show the values over bright surfaces will be approximately reduced by 8% and 18% when mineral dust is mixed with $w_s = 20\%$ of soot aggregates (Fig. 7). Furthermore, the results suggest that the SSA variance effect on TOA reflectance can be magnified by aerosol loading (i.e., AOD), and the influence contributed by SSA variance is quite similar between the different wavelengths of 0.412, 0.470, and $0.650 \mu\text{m}$ and over both dark and bright areas.

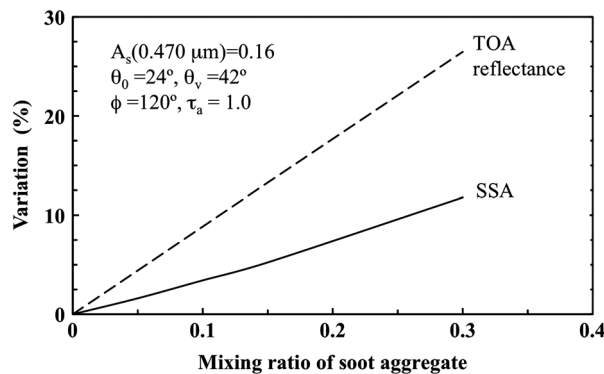


Fig. 7 The variations of simulated SSA and TOA reflectance at $0.470 \mu\text{m}$ together with different mixing weights of soot aggregates.

Table 1 Parameters for assessing the phase function effect on TOA reflectance by pure dust and a dust-soot mixture.

	Pure dust		Dust-soot mixture		Environment		
	Refractive index	SSA	Refractive index	SSA	Surface reflectance dark	Surface reflectance bright	AOD (τ_a)
0.412 μm	$1.55 + 0.006i$	0.923	$1.55 + 0.0020i$	0.926	0.04	0.08	1.0
0.470 μm	$1.55 + 0.004i$	0.946	$1.55 + 0.0005i$	0.941	0.08	0.16	1.0
0.650 μm	$1.55 + 0.002i$	0.973	$1.55 + 0.0005i$	0.969	0.15	0.30	1.0

4.2 Phase Function Variance on TOA Reflectance

To further assess the phase function influence, a set of the equivalent SSAs (less than 0.5% difference) calculated by the simulations in Sec. 3 is employed, as listed in Table 1. The dust-soot mixture phase function deviates substantially from its dust counterpart in the side-scattering and backscattering directions at 0.470 μm (with the difference ranging from 15% to 30%). A larger difference in the TOA reflectance may occur in the side- and backward-viewing directions between pure dust and polluted dust cases. To evaluate the influence of the phase function differences on the TOA reflectance, the simulations of the reflectance at the TOA at 0.470 μm over dark and bright surfaces are depicted in Fig. 8. Overall, the phase function variation influence on the TOA reflectance ranges from 0.7% to 7.0% when aerosol loading (AOD) is less than 2.0. The influence becomes more significant with increased AOD at shorter wavelengths (0.412 and 0.470 μm) and is noticeable, especially over darker surfaces. For the quantitative analyses, Table 2 summarizes the simulations of SSA and phase function (P_{11}) effects after mixing with soot aggregates on TOA reflectance (Figs. 6 and 8).

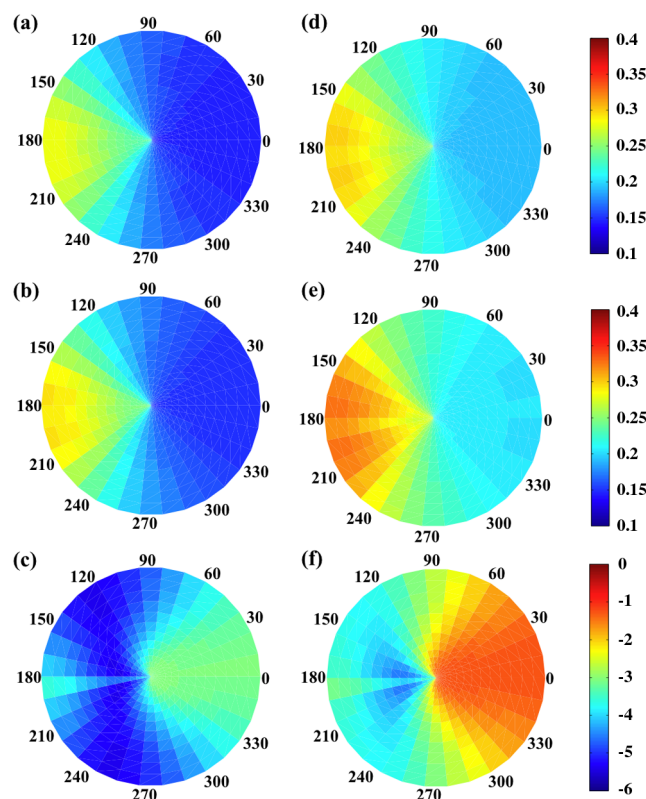

Fig. 8 Same as Fig. 7, but for the cases with equivalent SSA.

Table 2 The mean of relative difference in TOA reflectance between pure dust and dust-soot mixture over bright surface.

Wavelength	Surface reflectance	Soot weight	SSA variance from dust	P_{11} variance from dust	AOD	Mean difference of TOA reflectance (Min. ~ Max.)
0.412 μm	0.08	10%	3.8%	0.0023%	0.5	4.9% (3.6%–6.6%)
					1.0	8.8% (6.0%–10.6%)
					2.0	14.87% (9.4%–16.3%)
0.470 μm	0.16	10%	3.4%	0.0049%	0.5	4.9% (4.0%–6.8%)
					1.0	9.0% (7.2%–10.6%)
					2.0	15.3% (10.9%–16.6%)
0.650 μm	0.30	10%	2.6%	0.0002%	0.5	4.1% (3.1%–6.4%)
					1.0	7.5% (6.4%–9.5%)
					2.0	13.1% (10.4% - 14.5%)
0.412 μm	0.08	10%	0.3%	1.3%	0.5	2.2% (1.3%–4.2%)
					1.0	4.0% (2.7%–6.4%)
					2.0	6.6% (4.2%–8.8%)
0.470 μm	0.16	15%	0.5%	1.5%	0.5	1.4% (0.5%–3.7%)
					1.0	2.3% (1.3%–4.6%)
					2.0	3.4% (2.7%–5.3%)
0.650 μm	0.30	10%	0.4%	5.9%	0.5	0.1% (0.1%–1.8%)
					1.0	0.1% (0.4%–1.9%)
					2.0	0.04% (0.5%–1.8%)

Note: The mean difference of TOA reflectance is the average of viewing zenith (0 deg to 90 deg) and azimuth (0 deg to 180 deg) angles at 24 deg solar zenith.

5 AOD and SSA Retrievals with MODIS Data

Observations from the sun-photometer station (EMA_2 AERONET, 30.08°N, 31.29°E) located in Cairo, Egypt, indicate the aerosol content over the region includes a mixture of three individual components: background pollution by urban activities, biomass burning in the Nile Delta, and mineral dust from the desert regions (e.g., Sahara).^{58,59} Therefore, the Greater Cairo Region (GCR) is an area where aerosols from different origins are mixed in variable proportions, serving as a proper test site for the validation of the dust-soot mixture look-up tables constructed in this study. During two dust storm events, three MODIS observations around the megacity of Cairo were collected for examination of AOD and SSA retrievals of pure dust and dust-soot mixtures. The events include a pure-dust-like case (May 27, 2010) and two polluted-dust-like cases (May 16, 2010, and February 25, 2011) shown in Fig. 9. During the period from May 15 to 28, 2010, two dust storm events were recorded by the sun-photometer at Cairo_EMA_2 site (Fig. 10). The measurements of the aerosol optical properties indicated the dust plumes began to blow over the greater Cairo region with a slight loading on May 15 (e.g., small AOD value), and the concentration of dust particles was intensified by a storm on May 16 and 17 (see also Fig. 9). After May 18, the mineral dust characteristics could not be tracked (e.g., slight aerosol loading with relative large AE value) until a strong dust plume appeared on May 27. Accordingly, the MODIS/Aqua observations of May 16 and 27 are employed for the case studies; Case 1 for pure dust and Case 2 for polluted dust (dust-soot mixture). Case 3 is the dust storm

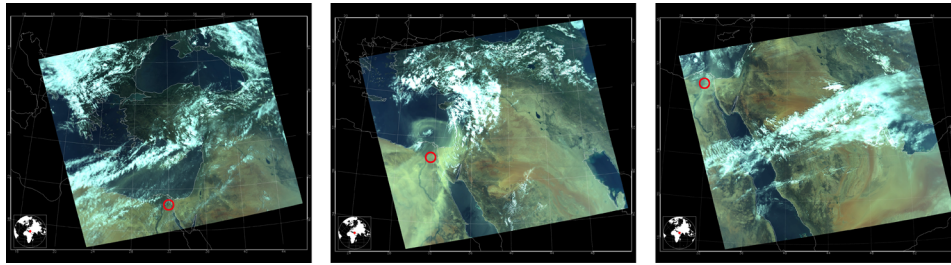


Fig. 9 MODIS images acquired on May 16, 2010 (left panel), May 27, 2010, (central panel) and February 25, 2011 (right panel). The red circles mark the target study area—the greater Cairo region.

event on February 25, 2011, similar to the May 16, 2010 polluted dust case, but with heavier dust aerosol loading, and additionally examined for polluted dust (dust-soot mixture).

With the MODIS land surface reflectivity products (MOD09, <http://lance.nasa.gov/data-products/modis-products/>) and the SSA retrieved from the Cairo_EMA_2 site (for the purpose of determining the mixing ratio of soot aggregates), the dust aerosol optical properties, AOD and SSA, can be retrieved from the MODIS apparent reflectance observed at the TOA based on the calculated look-up tables in this study.

For Case 1 corresponding to pure dust aerosol, the dust aerosol property retrievals from the look-up tables of the pure dust (dashed line in Fig. 11) are more accurate than those of

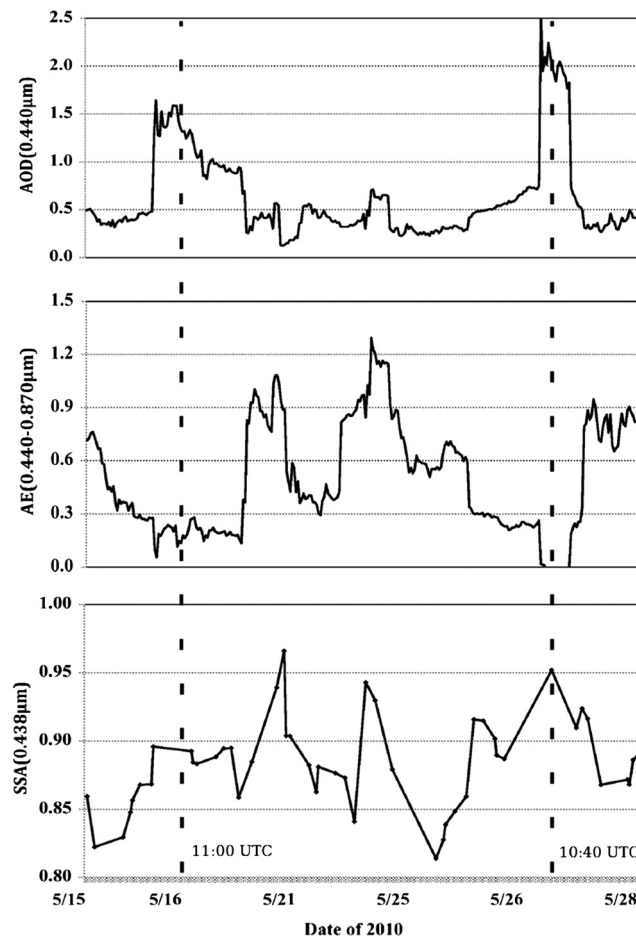


Fig. 10 The variations of AOD (top panel), AE (central panel) and SSA (bottom lower panel) from Cairo_EMA_2 site during May 15 to 28, 2010. Vertical dashed lines indicate the time of MODIS/Aqua observations.

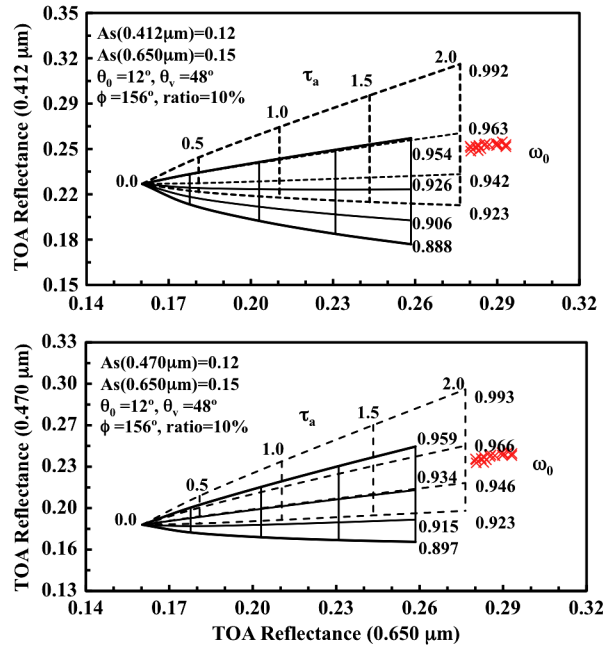


Fig. 11 Same as Fig. 3, but for different surface reflectivity and mixed with $w_s = 10\%$ soot aggregates. The red crosses represent the apparent reflectance from MODIS observations around the greater Cairo region on May 27, 2010 (Case 1).

the dust-soot mixture (solid line) in comparison with the sun-photometer measurements. The mean differences of the retrieved AOD and SSA between the pure dust look-up tables and the ground-based measurements are less than 1% (see also the Case 1 retrievals in Table 3), indicating that the proposed approach for retrieving dust aerosols is both highly reasonable and practical. Meanwhile, according to the spatial distribution of AOD and SSA retrievals over the greater Cairo region in Fig. 12, the AOD and SSA values are larger than 1.5 and 0.94, respectively, and have a homogenous distribution, which suggests a pure-dust-like case.

Table 3 The comparison of retrieved dust aerosols properties with and without soot aggregates over the greater Cairo region during the dust storm events.

Retrieval of dust aerosols	Sun photometer measurement	With soot aggregates	Without soot aggregates	MODIS products
Case 1- pure dust				
AOD	2.109 (0.440 μm)	2.426(+12.7%)	2.167(+0.7%)	1.520(-28.0%)
SSA	0.952 (0.438 μm) ^a	0.941(-1.2%)	0.947(-0.5%)	0.940(-1.3%)
Case 2- polluted dust				
AOD	1.316 (0.440 μm)	1.333(+1.3%)	1.159(-11.9%)	1.275(+3.1%)
SSA	0.895 (0.438 μm)	0.916(+2.4%)	0.932(+4.1%)	0.935(+4.5%)
Case 3- polluted dust				
AOD	1.595 (0.440 μm)	1.645(+3.3%)	1.459(-8.9%)	2.291(+48.4%)
SSA	0.916 (0.438 μm)	0.906(-1.1%)	0.909(-0.8%)	N/A

Note: The values of SSA retrieval are the mean of the results at the 0.412 and 0.470 μm bands, and the percentage in the bracket is the difference compared to the retrieval by the sun photometer measurement at Cairo_EMA_2 site.

^aNo observation available, the SSA value is assessed by the equivalent dust aerosol loading (AOD) during the spring of 2010.

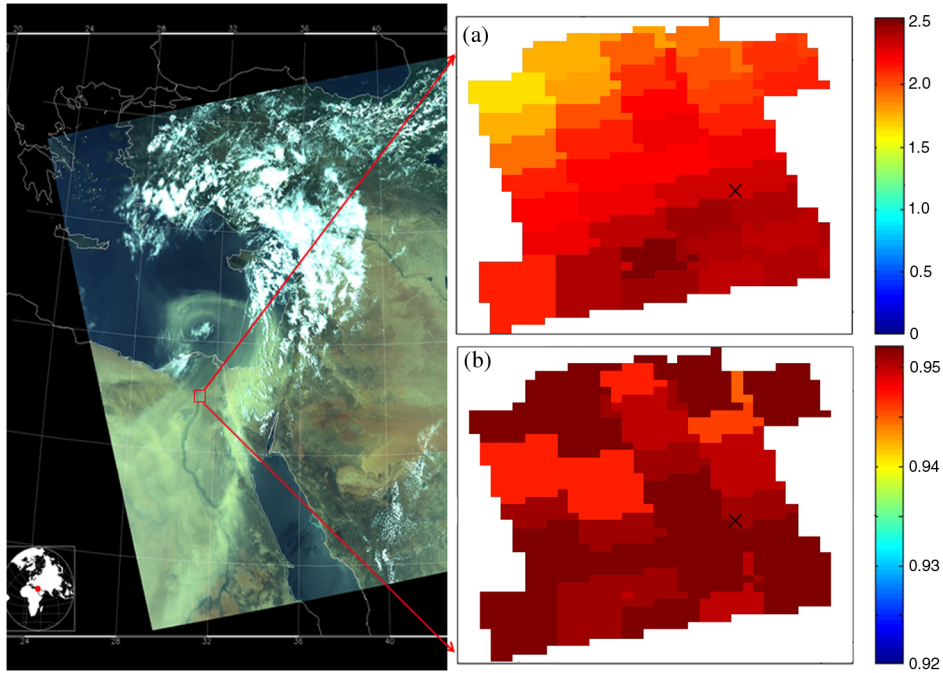


Fig. 12 (a) The spatial distributions of AOD and (b) SSA from the look-up tables of dust-soot mixtures over the greater Cairo region, MODIS/Aqua, May 27, 2010 (Case 1). The black cross indicates the location of the Cairo_EMA_2 site.

The Case 2 retrievals of polluted dust aerosol shown in Fig. 13 are more accurate than their pure dust counterparts. The differences between the retrieved AOD and SSA (based on the look-up tables indicated by the solid lines) and the ground-based measurements, are 1.3% and 2.4%, but the differences are as large as 11.9% and 4.1% (based on the look-up tables indicated by the dashed lines) if the effect of dust mixing with soot aggregates is neglected (see the Case 2 retrievals in Table 3). The results indicate that an overestimate of the SSA value will result in an underestimation of the AOD value. In Case 2, spatial distributions of AOD and SSA (Fig. 14) over the

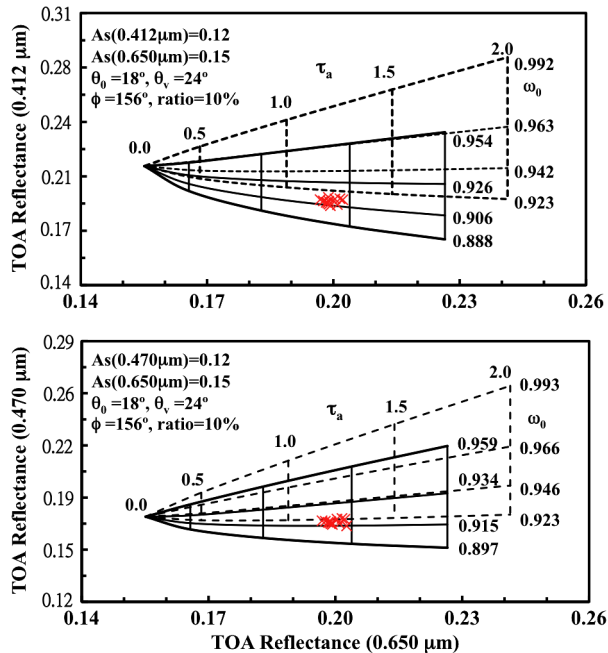


Fig. 13 Same as Fig. 11, but for Case 2 on May 16, 2010.

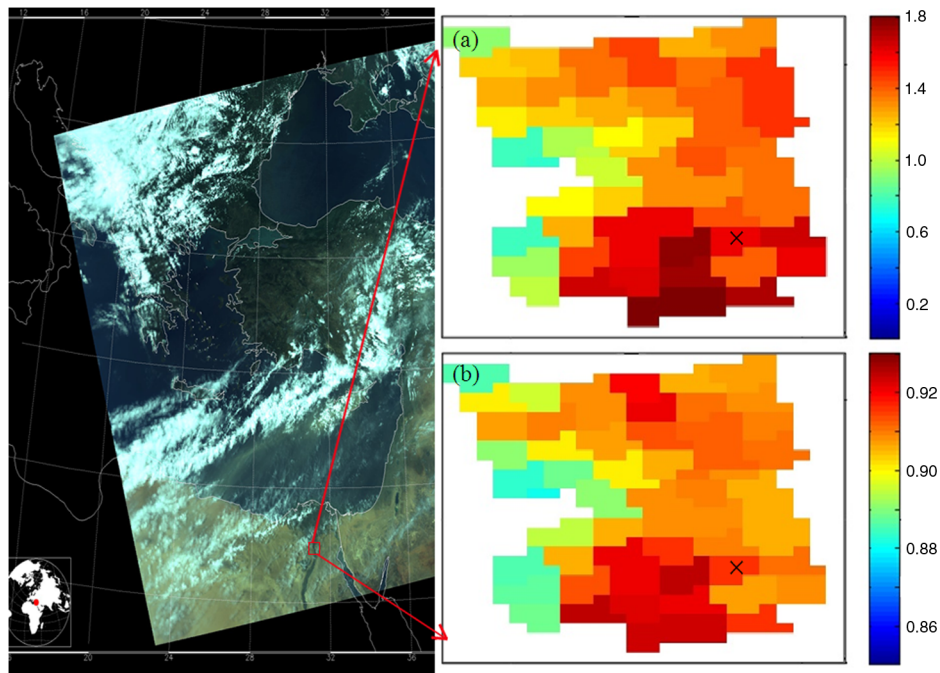


Fig. 14 Same as Fig. 12, but for Case 2 on May 16, 2010, based on the look-up tables of pure dust particles.

greater Cairo region decreases from the east to west side, and may describe the phenomenon of the dust plumes from the southeast gradually mixing with ambient aerosols (e.g., anthropogenic pollutants or smoke from biomass burning). The Case 3 results are similar and listed in Table 3.

6 Summary and Discussion

A simulation technique is applied to dust storm events observed by MODIS, aiming at evaluating the effect of dust mixing with soot aggregates on the dust particle optical properties. The look-up tables for retrieving the AOD and SSA of pure and polluted dust aerosols are constructed with a tri-axial ellipsoidal dust model and the GMM soot aggregation approach associated with the external mixing process. For validation, they are applied to MODIS data from three dust storm cases, one case for pure dust and two cases for the soot-contaminated dust. The results show the phase function of a dust-soot mixture with $w_s = 10\%$ soot weight to be almost the same as that of pure dust (less than 0.4% difference). The SSA differences are obvious (about 3%) because soot aggregates are strong absorbers of visible light. The apparent reflectance observed at the TOA is thus altered by the variations in the SSA and phase function, roughly 9.0% and 2.3% difference from pure dust at $0.470 \mu\text{m}$ over bright surfaces when AOD and soot mixing weight are assumed to be 1.0 and $w_s = 10\%$. The apparent reflectance variance results in a 20.0% and 1.2% difference for the AOD and SSA retrievals from pure dust.

With ancillary information about the surface reflectivity, the optical properties of mineral dust (AOD and SSA) can be retrieved from remotely sensed apparent reflectance. According to the results of the case studies from MODIS observations over the greater Cairo region, more accurate retrievals of pure dust and polluted dust properties are obtained on the basis of proposed look-up tables by means of the Deep Blue algorithm. In case of pure dust, both the AOD and SSA retrieval differences are less than 1% when compared with the ground-based measurements (AERONET). The errors of AOD and SSA retrievals of polluted dust are reduced from 11.9% to 1.3% and from 4.1% to 2.4%, respectively, if the lookup tables for pure dust are replaced by their counterparts for polluted dust with $w_s = 10\%$. This indicates that the external mixing process seems reasonable for the optical properties retrieved from satellite observations. Moreover, results from both the simulations and the case studies suggest that

by neglecting the mixing of dust aerosols with soot, the Deep Blue approach will underestimate the AOD retrieval and overestimate the SSA, and vice versa.

Acknowledgments

This study was partially supported by the endowment funds associated with the David Bullock Harris Chair in Geosciences, the College of Geosciences at Texas A&M University and NSF Grant ATM-0803779.

References

1. J. M. Prospero, "Long-range transport of mineral dust in the global atmosphere: Impact of African dust on the environment of the southeastern United States," *Proc. Natl. Acad. Sci. U. S. A.* **96**(7), 3396–3403 (1999), <http://dx.doi.org/10.1073/pnas.96.7.3396>.
2. J. Qiu and L. Yang, "Variation characteristics of atmospheric aerosol optical depths and visibility in North China during 1980–1994," *Atmos. Environ.* **34**(4), 603–609 (2000), [http://dx.doi.org/10.1016/S1352-2310\(99\)00173-9](http://dx.doi.org/10.1016/S1352-2310(99)00173-9).
3. Y. Ichikawa and S. Fujita, "An analysis of wet deposition of sulfate using a trajectory model for East Asia," *Water Air Soil Pollut.* **85**(4), 1927–1932 (1995), <http://dx.doi.org/10.1007/BF01186116>.
4. R. L. Arndt, G. R. Carmichael, and J. M. Roorda, "Seasonal source-receptor relationships in Asia," *Atmos. Environ.* **32**(8), 1397–1406 (1998), [http://dx.doi.org/10.1016/S1352-2310\(97\)00241-0](http://dx.doi.org/10.1016/S1352-2310(97)00241-0).
5. R. B. Husar et al., "Asian dust events of April 1998," *J. Geophys. Res.* **106**(D16), 18317–18330 (2001), <http://dx.doi.org/10.1029/2000JD900788>.
6. N. C. Hsu et al., "Deep blue retrievals of Asian aerosols properties during ACE-Asia," *IEEE Trans. Geosci. Remote Sens.* **44**(11), 3180–3195 (2006), <http://dx.doi.org/10.1109/TGRS.2006.879540>.
7. S. K. Satheesh and K. K. Moorthy, "Radiative effects of natural aerosols: a review," *Atmos. Environ.* **39**(11), 2089–2110, (2005), <http://dx.doi.org/10.1016/j.atmosenv.2004.12.029>.
8. M. O. Andreae and D. Rosenfeld, "Aerosol-cloud-precipitation interactions. Part 1. The nature and sources of cloud-active aerosols," *Earth-Sci. Rev.* **89**(1), 13–41 (2008), <http://dx.doi.org/10.1016/j.earscirev.2008.03.001>.
9. I. Uno et al., "Asian dust transported one full circuit around the globe," *Nat. Geosci.* **2**, 557–560 (2009), <http://dx.doi.org/10.1038/ngeo583>.
10. G.-R. Liu and T.-H. Lin, "Application of geostationary satellite observations for monitoring dust storms of Asia," *Terrest. Atmos. Ocean. Sci.* **15**(5), 825–837 (2004).
11. T.-H. Lin et al., "Asian dust weather categorization with satellite and surface observations," *Int. J. Rem. Sens.* **32**(1), 153–170 (2011), <http://dx.doi.org/10.1080/01431160903439932>.
12. J. Li, J. R. Anderson, and P. R. Buseck, "TEM study of aerosol particles from clean and polluted marine boundary layers over the North Atlantic," *J. Geophys. Res.* **108**(D6), 4189 (2003), <http://dx.doi.org/10.1029/2002JD002106>.
13. Y. Iwasaka et al., "Importance of dust particles in the free troposphere over the Taklamakan Desert: electron microscopic experiments of particles collected with a balloon-borne particle impactor at Dunhuang, China," *J. Geophys. Res.* **108**(D23), 8644 (2003), <http://dx.doi.org/10.1029/2002JD003270>.
14. H. J. Hwang and C.-U. Ro, "Direct observation of nitrate and sulfate formations from mineral dust and sea-salts using low-Z particle electron probe X-ray microanalysis," *Atmos. Environ.* **40**(2), 3869–3880 (2006), <http://dx.doi.org/10.1016/j.atmosenv.2006.02.022>.
15. Z. Shi et al., "Influences of sulfate and nitrate on the hygroscopic behavior of coarse dust particles," *Atmos. Environ.* **42**(4), 822–827 (2008), <http://dx.doi.org/10.1016/j.atmosenv.2007.10.037>.
16. Y. Iwasaka et al., "Mixture of Kosa (Asian dust) and bioaerosols detected in the atmosphere over the Kosa particles source regions with balloon-borne measurements: possibility of long-range transport," *Air Qual. Atmos. Health.* **2**(1), 29–38 (2009), <http://dx.doi.org/10.1007/s11869-009-0031-5>.

17. P. Yang et al., "Efficient finite-difference time domain scheme for light scattering by dielectric particles: application to aerosols," *Appl. Opt.* **39**(21), 3727–3737 (2000), <http://dx.doi.org/10.1364/AO.39.003727>.
18. O. V. Kalashnikova and I. N. Sokolik, "Modeling the radiative properties of nonspherical soil-derived mineral aerosols," *J. Quant. Spectrosc. Radiat. Transfer.* **87**(2), 137–166 (2004), <http://dx.doi.org/10.1016/j.jqsrt.2003.12.026>.
19. O. Dubovik et al., "Application of spheroid models to account for aerosol particle nonsphericity in remote sensing of desert dust," *J. Geophys. Res.* **111**(D11), 1–34 (2006), <http://dx.doi.org/10.1029/2005JD006619>.
20. Q. Feng et al., "Effects of particle nonsphericity and radiation polarization on retrieving dust properties from satellite observations," *J. Aerosol Sci.* **40**(9), 776–789 (2009), <http://dx.doi.org/10.1016/j.jaerosci.2009.05.001>.
21. J. M. Haywood and K. P. Shine, "The effect of anthropogenic sulfate and soot aerosol on the clear sky planetary radiation budget," *Geophys. Res. Lett.* **22**(5), 603–606 (1995), <http://dx.doi.org/10.1029/95GL00075>.
22. C. M. Sorensen and G. C. Roberts, "The prefactor of fractal aggregates," *J. Colloid Interface Sci.* **186**(2), 447–452 (1997), <http://dx.doi.org/10.1006/jcis.1996.4664>.
23. K. Tian et al., "Distribution of the number of primary particles of soot aggregates in a non-premixed laminar flame," *Combust Flame.* **138**, 195–198 (2004), <http://dx.doi.org/10.1016/j.combustflame.2004.04.008>.
24. L. Liu and M. I. Mishchenko, "Effects of aggregation on scattering and radiative properties of soot aerosols," *J. Geophys. Res.* **110**(D11), D11211 (2005), <http://dx.doi.org/10.1029/2004JD005649>.
25. P. Gwaze et al., "Comparison of three methods of fractal analysis applied to soot aggregates from wood combustion," *J. Aerosol Sci.* **37**(7), 820–838 (2006), <http://dx.doi.org/10.1016/j.jaerosci.2005.06.007>.
26. F. Liu et al., "Effects of primary soot particle size distribution on the temperature of soot particles heated by a nanosecond pulsed laser in an atmospheric laminar diffusion flame," *Int. J. Heat Mass Transfer.* **49**(3–4), 777–788 (2006), <http://dx.doi.org/10.1016/j.ijheatmasstransfer.2005.07.041>.
27. D. W. Mackowski, "A simplified model to predict the effects of aggregation on the absorption properties of soot particles," *J. Quant. Spectrosc. Radiat. Transfer.* **100**(1–3), 237–249 (2006), <http://dx.doi.org/10.1016/j.jqsrt.2005.11.041>.
28. H. Li et al., "Numerical accuracy of "equivalent" spherical approximations for computing ensemble-averaged scattering properties of fractal soot aggregates," *J. Quant. Spectrosc. Radiat. Transfer.* **111**(14), 2127–2132 (2010), <http://dx.doi.org/10.1016/j.jqsrt.2010.05.009>.
29. H. Volten et al., "Scattering matrices and reflectance spectra of forsterite particles with different size distributions," *J. Quant. Spectrosc. Radiat. Transfer.* **100**(1–3), 429–436 (2006), <http://dx.doi.org/10.1016/j.jqsrt.2005.11.074>.
30. O. Muñoz et al., "Experimental and computational study of light scattering by irregular particles with extreme refractive indices: hematite and rutile," *Astron. Astrophys.* **446**(2), 525–535 (2006), <http://dx.doi.org/10.1051/0004-6361:20053727>.
31. D. B. Curtis et al., "A laboratory investigation of light scattering from representative components of mineral dust aerosol at a wavelength of 550 nm," *J. Geophys. Res.* **113**(D8), 1–15 (2008), <http://dx.doi.org/10.1029/2007JD009387>.
32. M. I. Mishchenko, L. Travis, and A. Lacis, "Radiative transfer: scattering," in *Encyclopedia of Atmospheric Sciences*, J. R. Holton, J. Pyle, and J. A. Curry, Eds., Academic Press, San Diego (2003).
33. P. Yang et al., "Modeling of the scattering and radiative properties of nonspherical dust-like aerosols," *J. Aerosol Sci.* **38**(10), 995–1014 (2007), <http://dx.doi.org/10.1016/j.jaerosci.2007.07.001>.
34. T. X.-P. Zhao et al., "A study of the effect of non-spherical dust particles on the AVHRR aerosol optical thickness retrievals," *Geophys. Res. Lett.* **30**(6), 1317–1320 (2003), <http://dx.doi.org/10.1029/2002GL016379>.

35. M. Kahnert, T. Nousiainen, and P. Raisanen, "Mie simulations as an error source in mineral aerosol radiative forcing calculations," *Quarterly J. Royal Meteorol. Soc.* **133**(623), 299–307 (2007), [http://dx.doi.org/10.1002/\(ISSN\)1477-870X](http://dx.doi.org/10.1002/(ISSN)1477-870X).
36. M. I. Mishchenko et al., "Modeling phase functions for dustlike tropospheric aerosols using a mixture of randomly oriented polydisperse spheroids," *J. Geophys. Res.* **102**(D14), 16831–16847 (1997), <http://dx.doi.org/10.1029/96JD02110>.
37. L. Bi et al., "Single-scattering properties of triaxial ellipsoidal particles for a size parameter range from the Rayleigh to geometric-optics regimes," *Appl. Opt.* **48**(1), 114–126 (2009), <http://dx.doi.org/10.1364/AO.48.000114>.
38. Z. Meng et al., "Single-scattering properties of tri-axial ellipsoidal mineral dust aerosols: a database for application to radiative transfer calculations," *J. Aerosol Sci.* **41**(5), 501–512 (2010), <http://dx.doi.org/10.1016/j.jaerosci.2010.02.008>.
39. B. Yi et al., "Radiative transfer simulation of dust-like aerosols: uncertainties from particle shape and refractive index," *J. Aerosol Sci.* **42**(10), 631–644 (2011), <http://dx.doi.org/10.1016/j.jaerosci.2011.06.008>.
40. C. M. Sorensen, "Light scattering by fractal aggregates: a review," *Aerosol Sci. Technol.* **35**(2), 648–687 (2001), <http://dx.doi.org/10.1080/02786820117868>.
41. L. Liu and M. I. Mishchenko, "Scattering and radiative properties of complex soot and soot-containing aggregate particles," *J. Quant. Spectrosc. Radiat. Transfer.* **106**(1–3), 262–273 (2007), <http://dx.doi.org/10.1016/j.jqsrt.2007.01.020>.
42. L. Liu, M. I. Mishchenko, and W. P. Arnott, "A study of radiative properties of fractal soot aggregates using the superposition T-matrix method," *J. Quant. Spectrosc. Radiat. Transfer.* **109**(15), 2656–2663 (2008), <http://dx.doi.org/10.1016/j.jqsrt.2008.05.001>.
43. Y. L. Xu, "Calculation of the addition coefficients in electromagnetic multisphere-scattering theory," *J. Comput. Phys.* **127**(1), 285–298 (1996), <http://dx.doi.org/10.1006/jcph.1996.0175>.
44. Y. L. Xu and B. A. Gustafson, "A generalized multiparticle Mie-solution: further experimental verification," *J. Quant. Spectrosc. Radiat. Transfer.* **70**(4–6), 395–419 (2001), [http://dx.doi.org/10.1016/S0022-4073\(01\)00019-X](http://dx.doi.org/10.1016/S0022-4073(01)00019-X).
45. M. I. Mishchenko et al., "Scattering and radiative properties of semi-external versus external mixtures of different aerosol types," *J. Quant. Spectrosc. Radiat. Transfer.* **88**(1–3), 139–147 (2004), <http://dx.doi.org/10.1016/j.jqsrt.2003.12.032>.
46. J. F. De Haan, P. B. Bosma, and J. W. Hovenier, "The adding method for multiple scattering calculations of polarized light," *Astron. Astrophys.* **183**(2), 371–391 (1987).
47. A. V. Filippov, M. Zurita, and D. E. Rosner, "Fractal-like aggregates: relation between morphology and physical properties," *J. Colloid Interface Sci.* **229**(1), 261–273 (2000), <http://dx.doi.org/10.1006/jcis.2000.7027>.
48. K. W. Lee, "Change of particle size distribution during Brownian coagulation," *J. Colloid Interface Sci.* **92**(2), 315–325 (1983), [http://dx.doi.org/10.1016/0021-9797\(83\)90153-4](http://dx.doi.org/10.1016/0021-9797(83)90153-4).
49. G. A. D'Almeida, P. Keopke, and E. P. Shettle, *Atmospheric Aerosols: Global Climatology and Radiative Characteristics*, A. Deekpak Pub., Hampton (1991).
50. C. Levonie et al., "Atmospheric aerosol optical properties: a database of radiative characteristics for different components and classes," *Appl. Opt.* **36**(30), 8034–8041 (1997), <http://dx.doi.org/10.1364/AO.36.008031>.
51. M. Chin et al., "Aerosol distribution in the Northern Hemisphere during ACE-Asia: results from global model, satellite observations, and Sun photometer measurements," *J. Geophys. Res.* **109**(D23), D23S90 (2004), <http://dx.doi.org/10.1029/2004JD004829>.
52. T. F. Eck et al., "Columnar aerosol optical properties at AERONET sites in central eastern Asia and aerosol transport to the tropical mid-Pacific," *J. Geophys. Res.* **110**(D6), D06202 (2005), <http://dx.doi.org/10.1029/2004JD005274>.
53. D. Müller et al., "Mineral dust observed with AERONET Sun photometer, Raman lidar, and in situ instruments during SAMUM 2006: shape-independent particle properties," *J. Geophys. Res.* **115**(D11), D07202 (2010), <http://dx.doi.org/10.1029/2009JD012520>.
54. M. I. Mishchenko, A. A. Lacis, and L. D. Travis, "Errors introduced by the neglect of polarization in radiance calculations for Rayleigh scattering atmospheres," *J. Quant.*

- Spectrosc. Radiat. Transfer.* **51**, 491–510 (1994), [http://dx.doi.org/10.1016/0022-4073\(94\)90149-X](http://dx.doi.org/10.1016/0022-4073(94)90149-X).
55. R. C. Levy, L. A. Remer, and Y. J. Kaufman, “Effects of neglecting polarization on the MODIS aerosol retrieval over land,” *IEEE Trans. Geosci. Remote Sens.* **42**(11), 2576–2583 (2004), <http://dx.doi.org/10.1109/TGRS.2004.837336>.
 56. B. A. Bodhaine et al., “On Rayleigh optical depth calculations,” *J. Atmos. Oceanic Technol.* **16**(11), 1854–1861 (1999), [http://dx.doi.org/10.1175/1520-0426\(1999\)016<1854:ORODC>2.0.CO;2](http://dx.doi.org/10.1175/1520-0426(1999)016<1854:ORODC>2.0.CO;2).
 57. N. C. Hsu et al., “Aerosol properties over bright-reflecting source regions,” *IEEE Trans. Geosci. Remote Sens.* **42**(3), 557–569 (2004), <http://dx.doi.org/10.1109/TGRS.2004.824067>.
 58. M. El-Metwally et al., “Aerosol characteristics over urban Cairo: seasonal variations as retrieved from Sun photometer measurements,” *J. Geophys. Res.* **113**(D14), D14219 (2008), <http://dx.doi.org/10.1029/2008JD009834>.
 59. A. S. Zakey, M. M. Abdel Wahab, and P. A. Makar, “Atmospheric turbidity over Egypt,” *Atmos. Environ.* **38**(11), 1579–1591(2004), <http://dx.doi.org/10.1016/j.atmosenv.2003.12.017>.

Biographies and photographs of the authors not available.